Coherent Rayleigh-Brillouin scattering in molecular gases

Xingguo Pan, Mikhail N. Shneider, and Richard B. Miles*
Department of Mechanical and Aerospace Engineering, Princeton University, Princeton, New Jersey 08544, USA
(Received 18 June 2003; published 22 March 2004)

We present an experimental and theoretical study of the coherent Rayleigh-Brillouin scattering in gases in the kinetic regime. Gas density perturbation waves were generated by two crossing pump laser beams through optical dipole forces. A probe laser beam was then coherently scattered from the perturbation waves. The line shape of the scattered light was modeled using kinetic theory. The model takes into account the internal energy modes of the gas particles and is applicable to both molecular and atomic gases. We discuss the implication of coherent Rayleigh-Brillouin scattering on kinetic theory and photon matter interaction.

DOI: 10.1103/PhysRevA.69.033814 PACS number(s): 42.65.Es, 33.20.Fb, 42.50.Vk, 51.10.+y

I. INTRODUCTION

Nonlinear light scattering processes at nonresonant frequencies have been widely studied in liquids and gases. In such a process, the medium is first perturbed by crossing laser beams, and a probe beam is then scattered from the perturbed medium. Two examples in liquids are Brillouin enhanced four wave mixing [1] and the observation of the complex Brillouin spectrum [2]. In gases, the problems can be treated in two regimes: the hydrodynamics regime and the kinetic regime. They are defined using the y parameter, which represents the ratio between the scattering wavelength and the gas particles' mean free path. When y is large, the gas can be treated as a continuum and the scattering process can be modeled using the Navier-Stokes equations coupled with the Maxwell equations. The kinetic regime is defined where the scattering wavelength is comparable or smaller than the mean free path, with $0 \leqslant y \lesssim 5$. In this regime, kinetic equations and the Maxwell equations are generally used to study the scattering problem. She *et al.* [3,4] first observed the stimulated Rayleigh-Brillouin scattering in argon and SF_6. The differential detection technique they used can only partially resolve the Rayleigh peak. It is interesting that She *et al.* envisioned coherent Rayleigh-Brillouin scattering (CRBS) as it is performed in this article. In the last decade, the laser induced thermal acoustics (LITA) and laser induced electrostrictive gratings (LIEG) have been studied [5–7]. These techniques have been widely used in optical diagnostics. The theoretical framework of the above research efforts are generally based on the Navier-Stokes and Maxwell equations. In the collisionless limit of the kinetic regime, Grinstead and Barker [8] observed the line shape of coherent Rayleigh scattering. A theoretical line shape was obtained by solving a collisionless kinetic equation in the space time domain. In a previous letter [9], we reported coherent Rayleigh-Brillouin scattering (CRBS) in gases in the kinetic regime. Data in argon and krypton and a single parameter kinetic model were presented. CRBS contains coherent Rayleigh scattering and can be connected to phenomena in the hydrodynamic regime such as LIEG.

Previous works on spontaneous Rayleigh-Brillouin scattering provide a substantial foundation for the current work. In the kinetic regime, Yip and Nelkin [10] first developed a kinetic model with the linearized Bhatnagar-Gross-Krook collision term [11]. Boley *et al.* [12] and Tenti *et al.* [13] started from the linearized Wang-Chang–Uhlenbeck [14] equation and developed models for molecular gases. Their six moment model, popularly called the $s6$ model, has been considered the best model by several authors [15–17]. The modeling of the spontaneous Rayleigh-Brillouin line shape in the kinetic regime continues to attract interest. Recently, Marques, Jr. and co-workers presented extended kinetic models [18,19] and reported good agreement with experimental data. Rangel-Huerta and Velasco [20] extended the hydrodynamic equations into the kinetic regime to study the Rayleigh-Brillouin line shape in atomic gases. Most of these works can be extended to study nonlinear light scattering processes at nonresonant frequencies by incorporating the optical dipole force into the model.

In this article, we present experimental data in N_2, O_2, and CO_2. The details of the experiment are described. We also present a theoretical model of the CRBS line shape that takes into account the internal energy modes of the gas particles. This model is based on Wang-Chang–Uhlenbeck equation and follows the work of [12,13].

II. OVERVIEW

The physical process of CRBS is illustrated in Fig. 1. Two pump beams, both polarized perpendicular to the page, are focused and crossed at their foci. They form an interference pattern and generate a wavelike density perturbation field in the gas. A probe beam is then coherently scattered from the

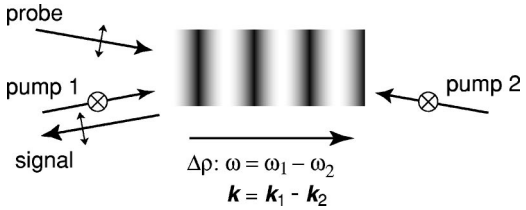

FIG. 1. Coherent Rayleigh-Brillouin scattering in gases.

*Electronic address: miles@princeton.edu

perturbation and forms the CRBS signal, which is also a beam.

It is through the optical dipole force that the pump beams generate the gas density perturbation. As discussed by Boyd [21], a molecule with polarizability α in an electric field E obtains a potential energy $U=-\frac{1}{2}\alpha|E|^2$. If the electric field is inhomogeneous, the tendency for the system to approach minimum potential energy manifests itself as the optical dipole force on the molecule $\boldsymbol{F}=-\nabla U$. Therefore, a molecule is pushed by the optical dipole force to the region where the field intensity is stronger.

The generated gas density perturbation has a coherent wave structure following the pump beams' interference pattern, as illustrated in Fig. 1. When the probe beam, counterpropagated against pump beam 2, is shone upon the density wave, it will be coherently scattered. The signal beam maintains the probe beam's polarization and follows a path determined by the phase matching condition:

$$\boldsymbol{k}_{\text{signal}}-\boldsymbol{k}_{\text{probe}}=\boldsymbol{k}=\boldsymbol{k}_1-\boldsymbol{k}_2, \tag{1}$$

where $\boldsymbol{k}_{\text{signal}}$ and $\boldsymbol{k}_{\text{probe}}$ are the wave vectors of the signal and the probe beams, respectively; $\boldsymbol{k}$ is the gas density wave vector; $\boldsymbol{k}_1$ and $\boldsymbol{k}_2$ are the wave vectors of the pump beams. The phase matching condition states the momentum conservation in this process. The process also maintains energy conservation, which is

$$\omega_{\text{signal}}-\omega_{\text{probe}}=\omega=\omega_1-\omega_2, \tag{2}$$

where ω_1 and ω_2 represent the frequencies of two single mode pump beams. The frequency of the CRBS signal ω_{signal} is shifted from that of the probe beam ω_{signal} by the frequency of the density perturbation wave ω. In this work, the gas density perturbation wave has a wavelength of about 256 nm and the frequency ω spans about 6 GHz.

The intensity of light scattered by a collection of scatterers is derived from the Maxwell equations [22]. The scattering results from the dielectric constant fluctuations $\delta\varepsilon$ of the medium, and the intensity of the scattered light is proportional to $\delta\varepsilon^2$. In fluids, the dielectric constant is generally a function of density and temperature [23]. In dilute gases, its dependency on temperature can be ignored and the dielectric constant fluctuation is proportional to gas density fluctuation. Thus, we have the intensity of the scattered light,

$$I_{sc}\propto \delta\rho\ ^2 I_{inc},$$

where $\delta\rho$ is the gas density fluctuation, and I_{inc} is the incident light intensity.

Based on the results in [9], one finds that $\delta\rho^2$ is proportional to the product of the pump lasers' intensity in CRBS. Therefore, the signal intensity in CRBS is

$$I_{\text{crbs}}\propto I_{\text{pump1}}I_{\text{pump2}}I_{\text{probe}}, \tag{3}$$

which is a general formula for a third order nonlinear optical process.

For an incident light whose power spectrum is a δ function, the power spectrum of the scattered light $S(\boldsymbol{k},\omega)$ is proportional to the spectral density of the dielectric constant fluctuations $S^{\epsilon}(\boldsymbol{k},\omega)$ [23]:

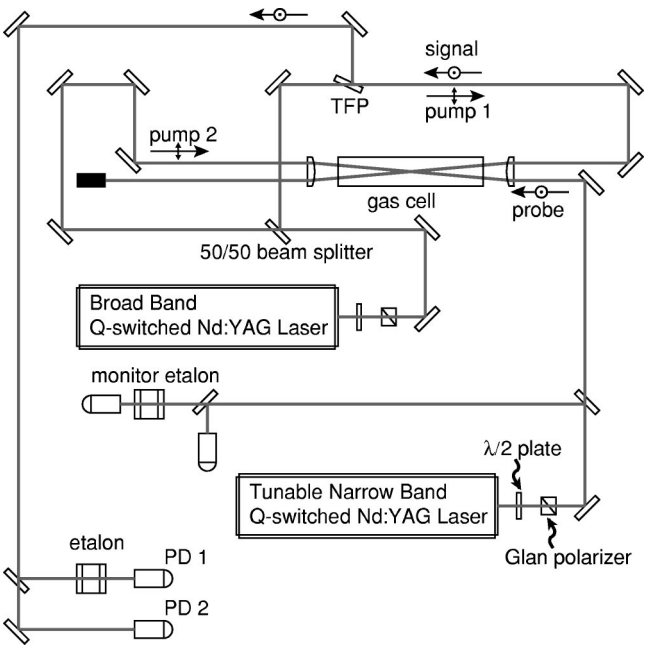

FIG. 2. The experimental setup of coherent Rayleigh-Brillouin scattering in gases.

$$S(\boldsymbol{k},\omega)\propto S^{\epsilon}(\boldsymbol{k},\omega)=\mathfrak{F}\{\langle\delta\epsilon^*(\boldsymbol{k},0)\,\delta\epsilon(\boldsymbol{k},t)\rangle\}, \tag{4}$$

where $\mathfrak{F}\{\}$ denotes Fourier transform and the time correlation of the dielectric constant fluctuation is defined as

$$\langle\delta\epsilon^*(\boldsymbol{k},0)\,\delta\epsilon(\boldsymbol{k},t)\rangle=\int\delta\epsilon^*(\boldsymbol{k},\tau)\,\delta\epsilon(\boldsymbol{k},\tau+t)\,d\tau.$$

We will look for a steady state solution to our problem. For such a solution, in which the direction of time does not play a role, the time correlation function equals its time convolution

$$\delta\epsilon^*(\boldsymbol{k},t)\ *\ \delta\epsilon(\boldsymbol{k},t)=\int\delta\epsilon^*(\boldsymbol{k},\tau)\,\delta\epsilon(\boldsymbol{k},t-\tau)\,d\tau.$$

Using the convolution theorem of Fourier transform in Eq. (4) and the relation $\delta\epsilon\propto\delta\rho$, we conclude that the coherent Rayleigh–Brillouin scattering power spectrum $S(\boldsymbol{k},\omega)$ is related to the gas density perturbation by

$$S(\boldsymbol{k},\omega)\propto\overline{\delta\rho}^*(\boldsymbol{k},\omega)\,\overline{\delta\rho}(\boldsymbol{k},\omega), \tag{5}$$

where

$$\overline{\delta\rho}(\boldsymbol{k},\omega)=\frac{1}{2\pi}\int\int e^{-i(\boldsymbol{k}\cdot\boldsymbol{r}-\omega t)}\,\delta\rho(\boldsymbol{r},t)\,d^3r\,dt \tag{6}$$

is the space-time Fourier transform of the gas density perturbation. Our task to find the power spectrum of the scattered light then becomes finding the gas density perturbation.

III. EXPERIMENT

The experimental setup is shown in Fig. 2. A Q-switched, frequency doubled, broad band, pulsed Nd:YAG laser was used to produce the two pump beams. The laser

beam was first passed through a half-wave plate and a Glan polarizer. The polarizer was used to set the polarization of the pump beams. Turning the half-wave plate allows one to control the beam power passing through the polarizer. In this way, the beams' pulse energy could be controlled while the pulse's temporal profile was maintained.

The pump laser beam was then split into two by a 50/50 beam splitter. The two pump beams were directed into a gas cell from opposite ends. They were focused by two planoconvex lens and were crossed at their foci in the gas cell. The path lengths of the two beams were carefully matched so that the two pulses reached the interaction volume simultaneously. The pump beam pulse had a duration of about 10 ns and the pulse energy directed into the interaction region was around 6 mJ/pulse for each beam.

The pump laser's power spectrum was measured using a plane-parallel Fabry-Perot etalon to have a full width at half maximum (FWHM) of 24.8 ± 2.5 GHz. There was also a 250 MHz longitudinal mode structure in the pump laser's power spectrum, which matched the laser's cavity length. This mode structure manifested itself in the raw profile of the scattered light. The pump beams' broad band power spectrum indicated that the gas density waves generated by them also had a broad band power spectrum, i.e., a continuous superposition of sinusoidal wave modes.

The probe laser was an injection seeded, frequency doubled, pulsed Nd:YAG laser. Its pulse duration was 7 ns. The laser was operated in a single longitudinal mode with an ~150 MHz band width.

The probe beam was also passed through a half-wave plate and a Glan polarizer, so that the beam's power could be controlled while its temporal profile was maintained. The probe beam's polarization was set perpendicular to that of the pump beams'. Therefore, the probe beam would not form an interference pattern with the pump beams, and complexities associated with this were avoided. In addition, since we used a counterpropagating scheme for pump beam 2 and the probe beam, a perpendicular polarization prevented the probe beam from the entering pump laser and vice versa.

The probe beam was then directed and focused onto the pump beams' crossing volume in the gas cell. Two 500 mm focal-length planoconvex lenses were used to focus the beams. The pump beams passed off-axis through the lenses and intersected at their foci at a 178° angle. The diameter of the focal region was about 200 μm. The probe beam was counterpropagated against pump beam 2. The arrival time of the probe pulse was adjusted relative to that of the pump pulses so that maximum signal was obtained. The optimal delay was about 1 ns. The jitter of the two lasers was each about 2 ns.

In the experiment, the overlap of the probe beam and pump beam 2 was achieved by aligning them so that both passed through two apertures located at different places along the path. Pump beam 1 was then fine tuned so that a strong signal was obtained. When the room was dark, the signal generated by a 1 mJ/pulse probe beam and 6 mJ/pulse pump beams in room air could be clearly seen by eye on a white card. The measured signal beam intensity at these conditions was less than 5 μJ. To avoid the complexity of gas density fluctuations generated by the probe and signal beams' interaction, we reduced the pulse energy of the probe beam to minimum level in the experiment.

The gas cell was a 5 cm diameter and 0.8 m long stainless steel tube with windows on both ends. Before each scan, the cell was evacuated and purged with the working gas several times before being charged to the desired pressure.

By the phase matching condition, the signal beam followed, in reverse, the path of pump beam 1. A thin film polarizer was used to separate the signal beam from pump beam 1. The signal beam was then propagated for 7 m in the laboratory to be detected. At this distance, the background ambient scattering of laser light from optical elements was greatly attenuated. Still, mirrors and lenses were carefully turned to keep surface reflections of laser beams away from the signal beam's direction.

The detection system was composed of two photodetectors and an air spaced plane-parallel Fabry-Perot etalon. The inward facing surfaces of the two etalon mirrors had a 99.6 % reflectivity at 532 nm. As calibrated by the manufacturer, the mirror set yielded a finesse of 215 at a test wavelength of 543 nm. One of the etalon mirrors was mounted on a piezoelectric mount. The three piezostacks were independently controlled by a ramp generator. The other mirror was mounted on a high precision hand adjustable mount. The entire etalon was put in an enclosure whose temperature was stabilized to within ± 0.1 K.

In the laboratory, the etalon was aligned using a HeNe laser at 632.8 nm. The HeNe beam was collimated and expanded to a 20 mm diameter. Coarse alignment was done by adjusting the high precision hand adjustable mounts. Fine alignment was performed using the ramp generator. The etalon mirror separation could be adjusted to fit the needs of the measurement task. For most scans of CRBS data in this paper, the free spectral range was set at 11.85 GHz.

The photodetectors were photomultiplier tubes (PMT). About 4 % of the signal beam was directed to a photodetector for normalizing purpose. We call it the normalizing PMT, and it corresponds to PD 2 in Fig. 2. The majority of the signal was sent into the etalon and the passed light was received by another PMT. This PMT corresponds to PD 1 in Fig. 2, and will be called the signal PMT. The output from both PMTs were sent to a gated averager and the data were collected by a computer.

In the experiment, the probe laser's frequency was scanned by scanning the voltage applied to the seed laser. For each frequency step, the ratio of the signal intensity detected by the signal PMT (the one after the etalon) to that by the normalizing PMT made a data point of the profile. Thirty shots were averaged for each frequency step.

The instrument function of the system had a full width at half maximum of 150 MHz. It was measured by sending the probe laser beam directly to the detector system and scanning the laser frequency.

Two approaches may be used to resolve the power spectrum of the signal beam. In the first approach, the etalon is scanned while fixing the probe laser's frequency. To scan the etalon, one changes the mirror separation by varying the electric voltage applied onto the piezoelectric stacks on which one of the mirrors is mounted. An alternative approach is to scan the probe laser while fixing the etalon mir-

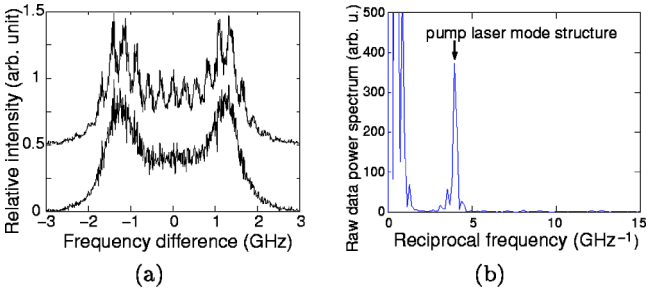

FIG. 3. (a) Raw CRBS data are shown by the upper curve, offset vertically by 0.5. The lower curve is the data after the mode structure is filtered, (b) the power spectrum of the raw experimental data.

ror separation. This is the approach used for most scans in this paper, mainly because the probe laser could be scanned at a higher resolution. Both approaches yield the same profile, which is a convolution of the signal beam's power spectrum and the etalon's transmission function.

As shown in Fig. 2, during each scan, part of the probe beam was directed to a monitor etalon. This monitor etalon was also an air spaced plane-parallel Fabry-Perot etalon, and its free spectral range was set to be 900 ± 0.2 MHz. When the probe laser frequency was scanned, there is a passband at every 900 MHz. These data were used to monitor the linearity of the frequency scan and to convert the control voltage applied on the seed laser to the probe beam's frequency shift.

The voltage applied to the seed laser V was converted to the frequency difference ν using the monitor etalon transmission profile of the probe beam. A program was written to identify the center of each passband. A quadratic relation between the frequency difference and the control voltage, $\nu = \nu_0 + aV + bV^2$, was fitted to the data. In general, the coefficient of the linear term a is much larger than the quadratic coefficient b, indicating good linearity of the scan. Still, a quadratic fitting of $\nu(V)$ is necessary to take care of the long term drifting of the frequency tuning.

The raw data of the coherent Rayleigh-Brillouin scattering profile are shown by the green curve in Fig. 3(a). A periodic, small amplitude modulation is clearly noticeable. It is due to the longitudinal mode structure of the pump laser. This mode structure can be seen more clearly in the data's power spectrum, shown in Fig. 3(b). The pump laser's mode structure is shown as the isolated, well defined peak around 4.0 GHz^{-1}. It shows that the pump laser's longitudinal modes are 250 MHz apart, a value that matched the pump laser's cavity length.

In the following section, we will compare the theoretical model and the experimental data for a pump force field that is constant in frequency. To accomplish this, we need to filter out the pump laser's mode structure from the raw data.

From the results of [9], and as will be confirmed later in this paper, the power spectrum of the scattering signal can be written as

$$S_{\mathrm{raw}}(\omega) = \beta \overline{F}(\omega) \ell_{\mathrm{crbs}}(\omega), \tag{7}$$

where β is a constant coefficient, $\overline{F}(\omega)$ is related to the power spectrum of the dipole force field, and $\ell_{\mathrm{crbs}}(\omega)$ is the coherent Rayleigh-Brillouin scattering line shape with a force field that is constant in the frequency domain. Ideally, one would like to have a force field uniform in frequency, i.e., $\overline{F}(\omega) = \mathrm{const}$. In our experiment, the force can be considered as a superposition of two components: one is a broad Gaussian profile with 24.8 GHz FWHM; the other is a periodic component representing the 250 MHz mode structure.

With a 24.8 GHz FWHM of the pump beam, the slowly changing component of the force varies less than 2% over the 6 GHz range of interest. We will therefore treat it as a constant over this range. We decompose the force as

$$\overline{F}(\omega) = \overline{F}_0 + \overline{F}_1(\omega), \tag{8}$$

where $\overline{F}_0$ is a constant and $\overline{F}_1(\omega)$ represents the mode structure.

We apply Fourier transform to Eq. (7):

$$\begin{aligned} \mathfrak{F}\{S_{\mathrm{raw}}(\omega)\} &= \mathfrak{F}\{(\overline{F}_0 + \overline{F}_1(\omega))\ell_{\mathrm{crbs}}(\omega)\} \\ &= \overline{F}_0 \mathfrak{F}\{\ell_{\mathrm{crbs}}(\omega)\} + \mathfrak{F}\{\overline{F}_1(\omega)\} * \mathfrak{F}\{\ell_{\mathrm{crbs}}(\omega)\}. \end{aligned} \tag{9}$$

The convolution term $\mathfrak{F}\{\overline{F}_1(\omega)\} * \mathfrak{F}\{\ell_{\mathrm{crbs}}(\omega)\}$ is well separated from the first term in the Fourier transform of the data, and is filtered out numerically. The filtered data are shown in Fig. 3(a) by the blue curve. The profile is a convolution of the coherent Rayleigh-Brillouin scattering line shape and the instrument function, and it will be compared with the theoretical line shape.

We have so far obtained data in argon, krypton, nitrogen, oxygen, and carbon . The argon and krypton data have been reported in [9,24]. The nitrogen, oxygen, and carbon dioxide data are shown in Figs. 4, 5, and 7 with the blue curve. The data present common characteristics. From $y \sim 0$ to $y \gtrsim 1$, the profile evolves from a near Gaussian curve to a curve with three distinctive peaks. For the line shape with a large y parameter, the central, unshifted, peak is due to the nonpropagating entropy fluctuations, and can be identified as the coherent Rayleigh peak. The position of the two side peaks corresponds to the speed of sound in the gas. The sidebands are due to the coherent sound waves generated by the optical dipole force field, and can be identified as the coherent Brillouin peaks. At larger y, the intensity ratio between the two Brillouin peaks and the Rayleigh peak keeps growing. This is different from the spontaneous Rayleigh-Brillouin scattering, where the ratio tends to a limit $c_v/(c_p - c_v)$ given by Landau and Placzek [25].

IV. A MODEL FOR COHERENT RAYLEIGH-BRILLOUIN SCATTERING IN MOLECULAR GASES

In [9], we presented a model for CRBS line shape of atomic gases. The perturbations on mass, momentum, and energy were solved from a linearized kinetic equation. The source of the perturbations is the optical dipole force field and the perturbations relax through collisions. The CRBS line shape of atomic gases was obtained analytically. It is found that the line shape in different gases scales with the y

parameter and the match between the model and the data is satisfactory. A step-by-step derivation of the model can be found in Chap. 3 of [26]. In this paper, we discuss a model of coherent Rayleigh–Brillouin scattering for molecular gases. We compare it with experimental data in nitrogen, oxygen, and carbon dioxide. Suppressing the internal energy modes, this model can be used for atomic gases as well.

The important difference between atomic gases and molecular gases is in a collision event. In an atomic gas, we only need to consider translational energy conservation. In a molecular gas, rotational and vibrational energy also need to be considered. We collectively call them internal energy. A collision event can be elastic, in which the total translational energy of the colliding particles is conserved, or it can be inelastic, in which translational energy is transferred into internal energy, or the other way around. We therefore need to find a kinetic equation that properly takes the internal energy levels into account. Wang-Chang, Uhlenbeck, and De Boer first proposed such a kinetic equation [14], which was successfully applied to problems such as transport coefficients [27,28], sound dispersion [29], and light scattering [12] in molecular gases. Following [14,28–30], Boley *et al.* [12] presented an eigentheory for the linearized Wang-Chang–Uhlenbeck equation. A model collision term was constructed using the eigentheory. They obtained a model for the spontaneous Rayleigh-Brillouin scattering line shape.

Our model for coherent Rayleigh-Brillouin scattering in molecular gases is an extension of the spontaneous Rayleigh-Brillouin scattering model by Boley *et al.* [12]. We add to the equation a source term due to the optical dipole force field and solve for the steady state solution. The solution procedure greatly resembles the atomic CRBS model presented in [9]. We will first linearize the WCU equation and use the model collision term. By taking the inner product of the linearized WCU equation and the eigenfunctions of the elastic collision operator, we obtain a linear equation set for the perturbed quantities (e.g., density, flow velocity, and temperature) in the Fourier domain. The perturbed quantities are then solved from this linear equation set. The line shape of the coherent Rayleigh-Brillouin scattering can therefore be calculated from the density perturbation.

We consider a gas whose molecular mass is M at temperature T and has N internal energy levels. The distribution function of the ith energy level is denoted by $f_i(\boldsymbol{v},\boldsymbol{r},t)$. In equilibrium, f_i follows the Boltzmann distribution, i.e.,

$$f_{i,\mathrm{eq}}(\boldsymbol{v},\boldsymbol{r},t) = n_0 x_i \phi(v), \tag{10}$$

where n_0 is the average number density, x_i is the fraction of molecules with internal energy E_i at the equilibrium state,

$$x_i = \frac{g_i e^{-E_i/k_b T}}{\sum_j g_j e^{-E_j/k_b T}}, \tag{11}$$

where g_i is the degeneracy of state i. $\phi(v)$ is the Maxwellian distribution

$$\phi(v) = \left(\frac{1}{\pi v_0^2}\right)^{3/2} \exp\left(-\frac{v^2}{v_0^2}\right), \tag{12}$$

where

$$v_0 = \sqrt{2k_b T/M}. \tag{13}$$

For such a gas, the full WCU equation is

$$\left(\frac{\partial}{\partial t} + \boldsymbol{v}\cdot\nabla + \boldsymbol{a}\cdot\nabla_v\right) f_i(\boldsymbol{v},\boldsymbol{r},t) = \sum_{jkl} \int (f_k' f_l' - f_i f_j)|\boldsymbol{v}-\boldsymbol{v}_1|\sigma_{ij}^{kl} d\Omega\, d^3 v_1. \tag{14}$$

This is a set of equations that describes the dynamics of the distribution function of each internal state. In this paper, we assume that the acceleration $\boldsymbol{a}$ of each molecule due to the optical dipole force does not depend on the internal state. This means that the polarizability of the gas particles does not change significantly for different internal states. The collision integral on the right hand side describes a collision between two particles. One is in the ith state before the collision, and has velocity $\boldsymbol{v}$. It transits to the kth state after the collision. The second particle is in the jth state before the collision and has velocity $\boldsymbol{v}_1$. It transits to the lth state after the collision. The collision cross section $\sigma_{ij}^{kl}(\boldsymbol{v},\boldsymbol{v}_1;\boldsymbol{v}',\boldsymbol{v}_1')$ depends on the internal energy levels involved in the collision, as well as the relative velocity of the two particles. Such a collision term includes the effects of elastic collisions, where $k=i$ and $l=j$, as well as inelastic collisions.

The derivation of WCU equation follows the same arguments used in the derivation of the Boltzmann equation. It is based on the assumptions that only binary collisions are important and that previous collisions do not influence subsequent collision probabilities (molecular chaos). As a result, the WCU equation satisfies the conservations of mass, momentum, and total energy. It also satisfies the H theorem. In addition, the principle of detailed balancing is assumed in the WCU equation. A possible weakness of the WCU equation is the assumption that there is no degeneracy in the internal energy levels. This sets $g_i=1$ in Eq. (11). The spatial degeneracy of rotational states (due to the orientation of the rotor) seems to pose a serious limit, however, for scalar problems such as density perturbation, the average effect of many collisions of the same kind is spherically symmetric. In this sense, the degeneracy of rotational states does not compromise the usefulness of WCU equations in scalar problems, as shown by its many successful applications.

The full, nonlinear, WCU equation is hard to handle. We now linearize it and use a model collision term to replace the collision integral. The material from here to Eq. (36) closely follows Boley *et al.* [12]. Notice that our definition of v_0 and several eigenfunctions are different. We write the distribution function of the ith internal level with a linearized deviation from the overall equilibrium as

$$f_i(\boldsymbol{v},\boldsymbol{r},t) = n_0 x_i \phi(v)[1 + h_i(\boldsymbol{v},\boldsymbol{r},t)], \tag{15}$$

where the deviation $h_i(\boldsymbol{v},\boldsymbol{r},t)$ is dimensionless and x_i and $\phi(v)$ have been given above.

The perturbation quantities that we are interested in can be expressed by the distribution function. These quantities include the deviation from equilibrium of the number densities of each internal state:

$$n_0 x_i \nu_i(\boldsymbol{r},t) = n_0 x_i \int \phi(v) h_i(\boldsymbol{v},\boldsymbol{r},t) d^3v, \tag{16}$$

the deviation of the total number density:

$$n_0 \nu(\boldsymbol{r},t) = n_0 \sum_i x_i \int \phi h_i d^3v, \tag{17}$$

the macroscopic flow velocity,

$$v_0 \boldsymbol{u}(\boldsymbol{r},t) = \sum_i x_i \int \boldsymbol{v} \phi h_i d^3v, \tag{18}$$

the deviation of the translational temperature,

$$T_0 \tau_{tr}(\boldsymbol{r},t) = \sum_i x_i \int \left(\frac{Mv^2}{3k_b} - T_0 \right) \phi h_i d^3v, \tag{19}$$

and the deviation of the internal temperature,

$$T_0 \tau_{\rm int}(\boldsymbol{r},t) = \frac{1}{k_b c_{\rm int}} \sum_i x_i \int (E_i - \langle E \rangle) \phi h_i d^3v, \tag{20}$$

where the angle brackets mean the average of all internal states, i.e.,

$$\langle E \rangle = \sum_i x_i E_i, \tag{21}$$

and the dimensionless internal specific heat capacity $c_{\rm int}$ is defined as

$$c_{\rm int} = \frac{1}{k_b} \frac{d\langle E \rangle}{dT_0} = \frac{\sum_i x_i (E_i - \langle E \rangle)^2}{(k_b T_0)^2}. \tag{22}$$

The deviation in total temperature $T_0\tau$ is then equal to the deviation of local average energy divided by $(3/2 + c_{\rm int})k_b$,

$$T_0 \tau(\boldsymbol{r},t) = \frac{T_0}{3/2 + c_{\rm int}} \left(\frac{3}{2} \tau_{tr} + c_{\rm int} \tau_{\rm int} \right). \tag{23}$$

The translation and internal heat flux are given by, respectively,

$$n_0 k_b T_0 v_0 \boldsymbol{q}_{tr} = n_0 \sum_i x_i \int \left(\frac{Mv^2}{2} - \frac{5k_b T_0}{2} \right) \boldsymbol{v} \phi h_i d^3v, \tag{24}$$

$$n_0 k_b T_0 v_0 \boldsymbol{q}_{\rm int} = n_0 \sum_i x_i \int (E_i - \langle E \rangle) \boldsymbol{v} \phi h_i d^3v. \tag{25}$$

In addition, the deviation of the traceless pressure tensor from equilibrium is given by

$$n_0 k_b T_0 \pi_{\alpha\beta} = n_0 M \sum_i x_i \int \left(v_\alpha v_\beta - \frac{1}{3} \delta_{\alpha\beta} v^2 \right) \phi h_i d^3v. \tag{26}$$

Assuming the perturbation is small, i.e., $h_i \ll 1$, we plug Eq. (15) into Eq. (14) to obtain the linearized WCU equation

$$\left(\frac{\partial}{\partial t} + \boldsymbol{v} \cdot \nabla \right) h_i - \frac{2}{v_0^2} \boldsymbol{a} \cdot \boldsymbol{v} = n_0 \sum_{jkl} x_j \int \int d^3v_1 d\Omega \phi(v_1) |\boldsymbol{v} - \boldsymbol{v}_1| \sigma_{ij}^{kl} \times [h_k(\boldsymbol{v}') - h_l(\boldsymbol{v}_1') - h_i(\boldsymbol{v}) - h_j(\boldsymbol{v}_1)]. \tag{27}$$

We have used the total energy conservation relation inside the collision integral and ignored higher order small terms $O(h_i^2)$. We have also applied the small perturbation approximation to the force term, which is

$$\frac{1}{\phi(v)} \boldsymbol{a} \cdot \nabla_v [\phi(v)(1 + h_i)] \approx \frac{1}{\phi(v)} \boldsymbol{a} \cdot \nabla_v \phi(v) = -\frac{2}{v_0^2} \boldsymbol{a} \cdot \boldsymbol{v}. \tag{28}$$

It is convenient to work on the problem in a Hilbert space. We choose to use the Dirac notations and write the column vector h_i as

$$|h\rangle = \begin{pmatrix} h_1 \\ h_2 \\ \vdots \end{pmatrix}. \tag{29}$$

The Hermitian conjugate of $|h_i\rangle$ is then a row vector

$$\langle h_i| = (h_1^*, h_2^*, \ldots, h_n^*).$$

The Hilbert space is based on the following definition of the inner product of vectors $\langle h|$ and $|h'\rangle$,

$$\langle h|h'\rangle \equiv \sum_i x_i \int \phi(v) h_i^*(\boldsymbol{v}) h_i'(\boldsymbol{v}) d^3v. \tag{30}$$

Using Dirac notation, Eq. (27) can be written as

$$\left(\frac{\partial}{\partial t} + \boldsymbol{v} \cdot \nabla \right) |h\rangle - \frac{2}{v_0^2} \boldsymbol{a} \cdot \boldsymbol{v} = n_0 J |h\rangle. \tag{31}$$

The collision operator J is an $N \times N$ matrix, and each element of this matrix is an integral operator. One can separate the operator J into its elastic and inelastic parts $J = J' + J''$. The elastic collision operator J' comes from the terms in Eq. (31) that have $k = i$ and $l = j$, and the inelastic operator consists of all other terms. Argument based on the symmetry of the elastic collision process leads to the conclusion that J' is a Hermitian operator with

$$\langle h|J'|h'\rangle = \langle h'|J'|h\rangle,$$

and the H theorem requires that

$$\langle h|J'|h'\rangle \leqslant 0, \quad \langle h|J''|h'\rangle \leqslant 0.$$

Wang-Chang and Uhlenbeck have found the eigenvectors and eigenvalues for the elastic collision operator J' for molecules that interact by the Maxwell force law $F_M = \kappa / r^5$, where r is the separation between the colliding molecules and the force constant κ is the same for all colliding pairs. In

this work, we assume that the gas molecules are Maxwellian molecules. The Maxwell force law is spherically symmetric, but molecules in general are not spherically symmetric. This seemingly contradictory assumption is again justified by the fact that the average cross section of numerous collisions is spherically symmetric.

The eigentheory of J' has been clearly explained by Boley *et al.* [12]. The reader is referred to [12,26] for detail. The eigenvectors are denoted by $|\Psi_{rlm,n}\rangle$. They are orthogonal to one another, i.e.,

$$\langle\Psi_{rlm,n}|\Psi_{r'l'm',n'}\rangle = \delta_{rr'}\delta_{ll'}\delta_{mm'}\delta_{nn'}. \tag{32}$$

The eigenvectors $\Psi_{rlm,n}$ span the entire Hilbert space, giving the completeness condition,

$$\sum_{rlmn} |\Psi_{rlm,n}\rangle\langle\Psi_{rlm,n}| = 1. \tag{33}$$

Explicitly, the eigenvector $\Psi_{rlm,n}$ is given by

$$\Psi_{rlm,n} = \begin{pmatrix} \Phi_{rlm}P_n(\varepsilon_1) \\ \Phi_{rlm}P_n(\varepsilon_2) \\ \vdots \end{pmatrix}, \tag{34}$$

where Φ_{rlm}'s are the eigenfunctions of the collision operator for an atomic gas with a Maxwell force law, or a gas with only one internal energy state. $P_n(\varepsilon_i)$ is a polynomial of the dimensionless internal energy $\varepsilon_i = E_i/k_bT_0$. The first two P_n's are given by

$$P_0(\varepsilon_i) = 1, \quad P_1(\varepsilon_i) = \frac{\varepsilon_i - \langle\varepsilon\rangle}{\sqrt{\langle(\varepsilon - \langle\varepsilon\rangle)^2\rangle}}.$$

Using the dimensionless velocity $\boldsymbol{c} = \boldsymbol{v}/v_0$, the function Φ_{rlm} is written explicitly as

$$\Phi_{rlm} = \sqrt{\frac{2\pi^{3/2}r!}{(r+l+1/2)!}} S^{(r)}_{l+1/2}(c^2)c^l Y_{lm}(\hat{c}), \tag{35}$$

where $S^{(m)}_n(x)$ is the Sonine polynomial and $Y_{lm}(\hat{c})$ is the spherical harmonics [31] given on the direction of the dimensionless velocity $\boldsymbol{c}$.

The first several Φ_{rlm}'s, which we will use, are

$$\Phi_{000} = 1, \quad \Phi_{010} = \sqrt{2}c_z,$$

$$\Phi_{100} = \sqrt{\frac{2}{3}}\left(\frac{3}{2} - c^2\right), \quad \Phi_{110} = \frac{2}{\sqrt{5}}\left(\frac{5}{2} - c^2\right)c_z,$$

$$\Phi_{020} = \frac{1}{\sqrt{3}}(3c_z^2 - c^2),$$

where the dimensionless velocity along z axis is $c_z = c\cos\theta$. The eigenvectors of J' we will be using include, with the subscripts denoting (rl,n), $\Psi_{00,0}$, $\Psi_{00,1}$, $\cdots$, $\Psi_{00,(N-1)}$, $\Psi_{01,0}$, $\Psi_{10,0}$, $\Psi_{11,0}$, $\Psi_{01,1}$, $\Psi_{02,0}$. These terms have clear physical meanings. The first N eigenvectors denote the fraction of particles in a specific internal state. $\Psi_{01,0}$ is the momentum, $\Psi_{10,0}$ is the translational energy term, $\Psi_{11,0}$ corresponds to translational heat flux, $\Psi_{00,1}$ is the internal energy, $\Psi_{01,1}$ is the internal heat flux, and $\Psi_{02,0}$ is the traceless pressure tensor. Only very limited knowledge of the eigentheory of the inelastic collision operator J'' is available. The five known eigenvectors all have an eigenvalue of zero. They are $\Psi_{000,0}$, $\Psi_{01m,0}$, and $-\Psi_{100,0} + \sqrt{2c_{int}/3}\Psi_{000,1}$, corresponding to the quantities that are conserved in an inelastic collision, i.e., mass, momentum, and total energy, respectively.

We use the collision model developed by Hanson and Morse [32] and Boley *et al.* [12]. It is constructed by the method of Gross and Jackson [33]. The collision model is the summation of the elastic and the inelastic models, given by

$$\begin{aligned}(J^{(7)}|h\rangle)_i = &- J'_{030}\nu_i - J''_{030}\nu - 2\boldsymbol{c}\cdot\boldsymbol{u}J_{030} + \tau_{tr}\left[(-J_{030}+J_{100})\left(c^2-\frac{3}{2}\right) - \frac{3}{2c_{\rm int}}J_{100}(\varepsilon_i - \langle\varepsilon\rangle)\right] \\ &+ \tau_{\rm int}\left[-J_{100}\left(c^2-\frac{3}{2}\right) + \left(\frac{3}{2c_{\rm int}}J_{100} - J''_{030}\right)(\varepsilon_i - \langle\varepsilon\rangle)\right] + 2\boldsymbol{c}\cdot\boldsymbol{q}_{tr}\left[(J_{110}-J_{030})\frac{2}{5}\left(c^2-\frac{5}{2}\right) - J^{110}_{011}\sqrt{\frac{2}{5c_{\rm int}}}(\varepsilon_i - \langle\varepsilon\rangle)\right] \\ &+ 2\boldsymbol{c}\cdot\boldsymbol{q}_{\rm int}\left[-J''^{110}_{011}\sqrt{\frac{2}{5c_{\rm int}}}\left(c^2-\frac{5}{2}\right) + (J_{011}-J_{030})\frac{\varepsilon_i - \langle\varepsilon\rangle}{c_{\rm int}}\right] + \pi_{\alpha\beta}(J_{020}-J_{030})\left(c_\alpha c_\beta - \frac{1}{3}\delta_{\alpha\beta}c^2\right) + J_{030}h_i,\end{aligned} \tag{36}$$

where J_{rln}'s, with or without primes and superscripts, are related to the eigenvalues. They are related to gasdynamics parameters through a Chapman-Enskog analysis. Details about J_{rln}'s can be found in [12,29].

Now we proceed to solve for the gas density perturbation from the linearized Wang-Chang–Uhlenbeck with a model collision term

$$\left(\frac{\partial}{\partial t} + \boldsymbol{v}\cdot\nabla\right)|h\rangle - \frac{2}{v_0^2}\boldsymbol{a}\cdot\boldsymbol{v} = n_0 J|h\rangle. \tag{37}$$

We seek for a steady state wavelike perturbation along the z axis of the form $\exp[-i(kz-\omega t)]$. The z axis is perpendicular to the fringes shown in Fig. 1. It is parallel to the direction of the optical dipole force and the density perturbation wave vector $\boldsymbol{k}$. We have $\boldsymbol{a}\cdot\boldsymbol{v} = av_z$ and $\boldsymbol{k}\cdot\boldsymbol{v} = kv_z$. An approximation is made to the pressure tensor term: We only keep the π_{zz} term and ignore other components of the tensor.

We will first apply a space time Fourier transform to Eq. (37), and then take the inner product, as defined by Eq. (30), of the transformed equation and the corresponding eigenvectors. We therefore obtain a system of seven linear equations of the physical quantities: $\nu(k,\omega)$, $u_z(k,\omega)$, $q_{tr,z}(k,\omega)$, $\pi_{zz}(k,\omega)$, $\tau_{tr}(k,\omega)$, $\tau_{\rm int}(k,\omega)$, $q_{{\rm int},z}(k,\omega)$.

The Fourier transform pair of gas density perturbation is

$$\nu(z,t)=\frac{1}{2\pi}\int \nu(k,\omega)\exp[i(kz-\omega t)]dkd\omega, \tag{38}$$

$$\nu(k,\omega)=\int \nu(z,t)\exp[-i(kz-\omega t)]dzdt. \tag{39}$$

The same transform is applied to the other six perturbed quantities, $|h\rangle$ and the acceleration $\boldsymbol{a}$. For simplicity, the same symbol is used for each Fourier pair, but they have different dimensions. For example, while $\nu(z,t)$ is dimensionless, $\nu(k,\omega)$ is of dimension [length/time]; and while $\boldsymbol{a}(z,t)$ is of dimension [length/time^{-2}], $\boldsymbol{a}(k,\omega)$ is of dimension [length^2/time^{-1}].

In the following, we use the dimensionless variables

$$\xi=\frac{\omega}{kv_0},\quad y_7=-\frac{nJ_{030}}{kv_0}. \tag{40}$$

Notice that, since $J_{030}\leqslant 0$, we have $y_7\geqslant 0$. It also proves convenient to define

$$I(\xi,y_7;c_z)=\frac{1}{\xi+iy_7-c_z}. \tag{41}$$

Taking the Fourier transform of Eq. (37) and multiplying both sides by $I(\xi,y_7;c_z)$, we obtain the kinetic equation for $|h\rangle$ in the frequency domain as

$$\begin{aligned}\frac{kv_0}{in_0}|h\rangle = I(\xi,y_7;c_z)\Bigg\{&-J'_{030}|\nu\rangle-J''_{030}\nu|\Psi_{000,0}\rangle-J_{030}\sqrt{2}u_z|\Psi_{010,0}\rangle+\left[J_{100}\sqrt{\frac{3}{2}}\tau_{\rm int}+(J_{030}-J_{100})\sqrt{\frac{3}{2}}\tau_{tr}\right]|\Psi_{100,0}\rangle\\&+\left[-J_{100}\frac{3}{2\sqrt{c_{\rm int}}}(\tau_{tr}-\tau_{\rm int})-J''_{030}\sqrt{c_{\rm int}}\tau_{\rm int}\right]|\Psi_{000,1}\rangle+\left[(-J_{030}+J_{011})\sqrt{\frac{2}{c_{\rm int}}}q_{{\rm int},z}-J^{110}_{011}\frac{2}{\sqrt{5}}q_{tr,z}\right]|\Psi_{010,1}\rangle\\&+\left[-(J_{110}-J_{030})\frac{2}{\sqrt{5}}q_{tr,z}+J^{110}_{011}\sqrt{\frac{2}{c_{\rm int}}}q_{{\rm int},z}\right]|\Psi_{110,0}\rangle+(J_{020}-J_{030})\frac{1}{\sqrt{3}}\pi_{zz}|\Psi_{020,0}\rangle+\frac{\sqrt{2}a}{n_0v_0}|\Psi_{010,0}\rangle\Bigg\},\end{aligned} \tag{42}$$

where, the gas perturbation vector $|\nu\rangle=\text{col}\,\{\nu_1,\nu_2,\ldots\}$. The equation has been sorted using the eigenvectors of the elastic collision operator.

Taking the inner product of Eq. (42) and $|\Psi_{000,0}\rangle=\text{col}\,(1,1,\ldots)$, we obtain the mass equation. Taking the inner product of Eq. (42) and $|\Psi_{010,0}\rangle=\sqrt{2}c_z\text{col}\,(1,1,\ldots)$, we obtain the momentum equation. Similarly, one can work out the other five equations. The result is shown below by the matrix equation Eq. (43):

$$AX=B, \tag{43}$$

with

$$A=\frac{n_0}{kv_0}\begin{pmatrix}
-J_{030}I^{00}_{00}-\frac{kv_0}{in_0} & -J_{030}I^{00}_{01} & (J_{030}-J_{110})I^{00}_{11} & (J_{020}-J_{030})I^{00}_{02} & (J_{030}-J_{100})I^{00}_{10} & J^{001}_{100}I^{00}_{10} & J^{110}_{011}I^{00}_{11}\\
-J_{030}I^{01}_{00} & -J_{030}I^{01}_{01}-\frac{kv_0}{in_0} & (J_{030}-J_{110})I^{01}_{11} & (J_{020}-J_{030})I^{01}_{02} & (J_{030}-J_{100})I^{01}_{10} & J^{001}_{100}I^{01}_{10} & J^{110}_{011}I^{01}_{11}\\
-J_{030}I^{11}_{00} & -J_{030}I^{11}_{01} & (J_{030}-J_{110})I^{11}_{11}+\frac{kv_0}{in_0} & (J_{020}-J_{030})I^{11}_{02} & (J_{030}-J_{100})I^{11}_{10} & J^{001}_{100}I^{11}_{10} & J^{110}_{011}I^{11}_{11}\\
-J_{030}I^{02}_{00} & -J_{030}I^{02}_{01} & (J_{030}-J_{110})I^{02}_{11} & (J_{020}-J_{030})I^{02}_{02}-\frac{3kv_0}{i2n_0} & (J_{030}-J_{100})I^{02}_{10} & J^{001}_{100}I^{02}_{10} & J^{110}_{011}I^{02}_{11}\\
-J_{030}I^{10}_{00} & -J_{030}I^{10}_{01} & (J_{030}-J_{110})I^{10}_{11} & (J_{020}-J_{030})I^{10}_{02} & (J_{030}-J_{100})I^{10}_{10}+\frac{kv_0}{in_0} & J^{001}_{100}I^{10}_{10} & J^{110}_{011}I^{10}_{11}\\
0 & 0 & -J^{110}_{011}I^{00}_{01} & 0 & -J^{001}_{100}I^{00}_{00} & (J_{001}-J_{030})I^{00}_{00}-\frac{kv_0}{in_0} & (J_{011}-J_{030})I^{00}_{01}\\
0 & 0 & -J^{110}_{011}I^{01}_{01} & 0 & -J^{001}_{100}I^{01}_{00} & (J_{001}-J_{030})I^{01}_{00} & (J_{011}-J_{030})I^{01}_{01}-\frac{kv_0}{in_0}
\end{pmatrix},$$

$$X=\begin{pmatrix}\nu\\ \sqrt{2}u_z\\ (2/\sqrt{5})q_{tr,z}\\ (1/\sqrt{3})\pi_{zz}\\ \sqrt{3/2}\tau_{tr}\\ \sqrt{c_{int}}\tau_{int}\\ (\sqrt{2/c_{int}})q_{int,z}\end{pmatrix},\quad B=-\frac{\sqrt{2}a}{kv_0^2}\begin{pmatrix}I_{01}^{00}\\ I_{01}^{01}\\ I_{01}^{11}\\ I_{01}^{02}\\ I_{01}^{10}\\ 0\\ 0\end{pmatrix}.$$

We have used the relation,

$$J_{100}=\sqrt{\frac{2c_{\rm int}}{3}}J_{100}^{001}=\sqrt{\frac{2c_{\rm int}}{3}}J_{001}^{100}=\frac{2c_{\rm int}}{3}J_{001},\qquad(44)$$

to write the matrix elements $A(6,5)$, $A(7,5)$ and the sixth column of A in a concise form. This relation comes from the fact that the collision operator is Hermitian and the total energy is conserved in a collision.

It is interesting to compare our equation with Eq. (43) of Boley *et al.* [12]. Our matrix A is essentially the same as Boley *et al.*'s. The sign difference in columns 3 and 5 and element $A(4,4)$ is due to different choices of the eigenvectors Φ_{100}, Φ_{110}, and Φ_{020}. Boley's choices resulted in a concise formula, while ours follow Eq. (35) and preserve the orthornormalilty of the eigenvectors. As long as the calculation of the $I_{rl}^{r'l'}$ is consistent with one's choice of the eigenfunctions, the results about the perturbation quantities such as $\nu(\omega,k)$ are the same.

Using our notation, the spontaneous Rayleigh-Brillouin scattering would have a B vector as

$$B_{spt}=-\frac{1}{k^2v_0}\begin{pmatrix}I_{00}^{00}\\ I_{00}^{01}\\ I_{00}^{11}\\ I_{00}^{02}\\ I_{00}^{10}\\ 0\\ 0\end{pmatrix}.\qquad(45)$$

This will be used later, when we compare our calculation of the spontaneous Rayleigh-Brillouin line shape with Tenti *et al.*'s.

In order to solve from Eq. (43) the gas density perturbation $\nu(\omega,k)$ and other physical quantities of interest, we need to calculate $J_{rln}^{r'l'n'}$'s and $I_{rl}^{r'l'}$'s. $J_{rln}^{r'l'n'}$'s are determined by four gas parameters through a Chapman-Enskog analysis. This has been done by Hanson and Morse [32] and Boley *et al.* [12]. The gas parameters include the shear viscosity η, bulk viscosity η_b, heat conductivity σ, and the dimensionless internal specific heat capacity $c_{\rm int}$ as defined in Eq. (22).

For computation purposes, it is convenient to use dimensionless quantities: the dimensionless internal heat capacity $c_{\rm int}$, the y parameter, the internal relaxation number $R_{\rm int}$, and the Eucken factor f_u. The latter three are given by

$$y=\frac{n_0k_bT_0}{\eta kv_0},\quad R_{\rm int}=\frac{3}{2}\frac{\eta_b}{\eta}\frac{(3/2+c_{\rm int})}{c_{\rm int}},$$

$$f_u=\frac{M\sigma}{\eta k_b(3/2+c_{\rm int})}.\qquad(46)$$

In terms of the dimensionless numbers, we rewrite the relations between $J_{rln}^{r'l'n'}$'s and the gasdynamic quantities as

$$\frac{n_0}{kv_0}J_{020}=-y,\quad \frac{n_0}{kv_0}J_{030}=-\frac{3}{2}y,$$

$$\frac{n_0}{kv_0}J_{100}=-\frac{y}{R_{\rm int}}\frac{c_{\rm int}}{3/2+c_{\rm int}},\qquad(47)$$

$$\frac{n_0}{kv_0}J_{110}=-\frac{2}{3}y-\frac{5}{6}\frac{y}{R_{\rm int}}\frac{c_{\rm int}}{3/2+c_{\rm int}},$$

$$\frac{n_0}{kv_0}J_{011}^{110}=-\sqrt{\frac{5}{8c_{\rm int}}}\frac{y}{R_{\rm int}}\frac{c_{\rm int}}{3/2+c_{\rm int}},$$

$$\frac{n_0}{kv_0}J_{011}=-\frac{2}{3}y\frac{c_{\rm int}}{3/2+c_{\rm int}}\frac{\frac{2}{5}\left(\frac{3}{2}+c_{\rm int}\right)+\frac{3+c_{\rm int}}{2R_{\rm int}}+\frac{9f_u}{16R_{\rm int}^2}}{-1+\frac{4}{15}f_u\left(\frac{3}{2}+c_{\rm int}\right)+\frac{c_{\rm int}f_u}{3R_{\rm int}}}.$$

From these relations, one can see that $y_7=3y/2$.

$I_{rl}^{r'l'}(\xi,y_7)$'s in Eq. (43) are defined by

$$I_{r'l'}^{rl}(\xi,y_7)\equiv\int\phi(v)I(\xi,y_7;c_z)\Phi_{rl0}(v)\Phi_{r'l'0}(v)d^3v.\qquad(48)$$

Before calculating $I_{rl}^{r'l'}(\xi,y_7)$'s, we discuss the integration

$$w_j(Z)=\int_{-\infty}^{+\infty}\frac{t^j\exp(-t^2)}{Z-t}dt,\quad j=0,1,2,\ldots,\qquad(49)$$

where Z is a complex variable in the first or second quadrant. $w_0(Z)$ is the plasma dispersion function multiplied by $(-\sqrt{\pi})$ [34]. Simple relations exist for w_j's, and the following were used in the computation:

$$w_1=-\sqrt{\pi}+Zw_0,\quad w_2=Zw_1,$$

$$w_3=-\frac{\sqrt{\pi}}{2}+Zw_2,\quad w_4=Zw_3,$$

$$w_5=-\frac{3}{4}\sqrt{\pi}+Zw_4,\quad w_6=Zw_5.$$

After completing the integration over the radial velocity components, $I_{rl}^{r'l'}(\xi,y_7)$'s are represented with $w_j(Z=\xi+iy_7)$ as

$$I_{00}^{00}=\frac{1}{\sqrt{\pi}}w_0,\quad I_{02}^{02}=\frac{2}{3\sqrt{\pi}}(w_0-2w_2+2w_4),$$

$$I_{00}^{01}=\sqrt{\frac{2}{\pi}}w_1,\quad I_{02}^{10}=\frac{1}{3\sqrt{2\pi}}(w_0+4w_2-4w_4),$$

$$I_{00}^{02}=\frac{1}{\sqrt{3\pi}}(-w_0+2w_2),\quad I_{00}^{10}=\frac{1}{\sqrt{6\pi}}(-w_0+2w_2),$$

$$I_{01}^{01}=\frac{2}{\sqrt{\pi}}w_2,\quad I_{02}^{11}=\frac{1}{\sqrt{15\pi}}(-w_1+8w_3-4w_5),$$

$$I_{10}^{10}=\frac{1}{6\sqrt{\pi}}(5w_0-4w_2+4w_4), \tag{50}$$

$$I_{00}^{11}=\frac{1}{\sqrt{5\pi}}(-3w_1+2w_3),\quad I_{01}^{02}=\sqrt{\frac{2}{3\pi}}(-w_1+2w_3),$$

$$I_{10}^{11}=\frac{1}{\sqrt{30\pi}}(7w_1-8w_3+4w_5),$$

$$I_{01}^{10}=\frac{1}{\sqrt{3\pi}}(-w_1+2w_3),\quad I_{01}^{11}=\sqrt{\frac{2}{5\pi}}(-3w_2+2w_4),$$

$$I_{11}^{11}=\frac{1}{5\sqrt{\pi}}(13w_2-12w_4+4w_6).$$

With Eqs. (47) and (50), we can solve the matrix Eq. (43). The solution is

$$X=A^{-1}B, \tag{51}$$

where A^{-1} is the inverse matrix of A and both are dimensionless. We see that the gas density perturbation $\nu(\xi,y)$ is a product of a/kv_0^2 and a part independent of the force. Using the relation between the gas density perturbation and the power spectrum of the scattered light, we obtain the CRBS line shape

$$S(\xi,y)\propto n_0^2\nu^*(\xi,y)\nu(\xi,y)\propto\left(\frac{n_0a}{kv_0^2}\right)^2\ell_{\mathrm{crbs}}(\xi,y;c_{\mathrm{int}},R_{\mathrm{int}},f_u). \tag{52}$$

This general relation is similar to that obtained in the atomic gas model [9]. It is a product of two factors: the first factor containing $a(\xi,y)^2$ is related to the power spectrum of the pump field; the second factor $\ell_{\mathrm{crbs}}(\xi,y;c_{\mathrm{int}},R_{\mathrm{int}},f_u)$ is a function of the y parameter as well as other gasdynamics parameters, but is independent of the optical dipole force. For a pump beam constant in the frequency range of interest, the CRBS signal power spectrum reveals the force independent part $\ell_{\mathrm{crbs}}(\xi,y;c_{\mathrm{int}},R_{\mathrm{int}},f_u)$. This property was used in Sec. III to filter out the pump beams mode structure from the raw data. We conclude that, in the perturbation regime, the CRBS line shape is independent of the pump beams' intensity.

TABLE I. A list of gas dynamic quantities of gases at $T_0=292$ K.

Gas	η (Pa s)	η_b/η	σ (W m^{-1} K-1)	c_{int}
N_2	17.63×10^{-6}	0.73	25.2×10^{-3}	1.0
O_2	20.21×10^{-6}	0.4	25.76×10^{-3}	1.0
CO_2	14.6×10^{-6}	$\sim$1000	16.2×10^{-3}	2.0

Because we have kept seven physical quantities in the above derivation, we call the model given by Eqs. (43), (47), (50), and (51) the seven moment model, or, the $s7$ model. We are also interested in a six moment model, called the $s6$ model, which does not include the traceless pressure tensor $\pi_{\alpha\beta}$. We can obtain the $s6$ model by repeating the derivation as with the $s7$ model or we can obtain it by reducing Eqs. (43) and (45) directly. We delete the fourth row and the fourth column of matrix A, and change all J_{030} into J_{020} in matrix A. The deleted elements are associated with the traceless pressure tensor element π_{zz}. We also delete the fourth elements in vectors X and B. The calculation of $I_{rl}^{r'l'}$ will be changed accordingly. In the $s7$ model, we have $I_{rl}^{r'l'}(\xi,y_7)$ as defined by Eqs. (41) and (48). In the six moment model, we have $I_{rl}^{r'l'}(\xi,y)$, replacing y_7 with y in Eq. (41).

We now compare the model with experimental data in nitrogen (N_2), oxygen (O_2), and carbon dioxide (CO_2). The gasdynamic parameters needed by the model are listed in Table I for $T_0=292$ K. The shear viscosity and heat conductivity data were found from the CRC handbook [35] and interpolated at the temperature. The bulk viscosity data of nitrogen were found in [13,36–38], of oxygen in [39,40], of carbon dioxide in [37].

Among these, the bulk viscosity η_b is a controversial parameter [37,41]. Bulk viscosity originates from the equilibration of internal energy and translational energy. It is well defined only when the time scale of the relaxation process is much shorter than the characteristic time of the system. In atomic gases, due to the decoupling of internal and translational energy modes, the bulk viscosity is zero. In molecular gases, the bulk viscosity is nonzero, but there are only a limited number of experimental measurements [36,39]. These measurements were based on sound wave dissipation and are in the frequency range of several megahertz. Partially because of this shortage of η_b data, the Stokes hypothesis, $\eta_b=0$, is widely used in fluid dynamics calculations. Our experiment corresponds to a GHz frequency regime. The definition and the value of the bulk viscosity in this regime may need further study.

In Fig. 4, we compare the seven moment model with the experimental data for nitrogen. The blue curve is the experimental data. The red curve is a convolution of the theoretical line shape and the instrument function. The only adjustment was to match the height of the curves. The model matches the experimental data reasonably well for the 1 and 4 atm data, but underestimated the relative height of the Rayleigh peak for the 2 and 3 atm data.

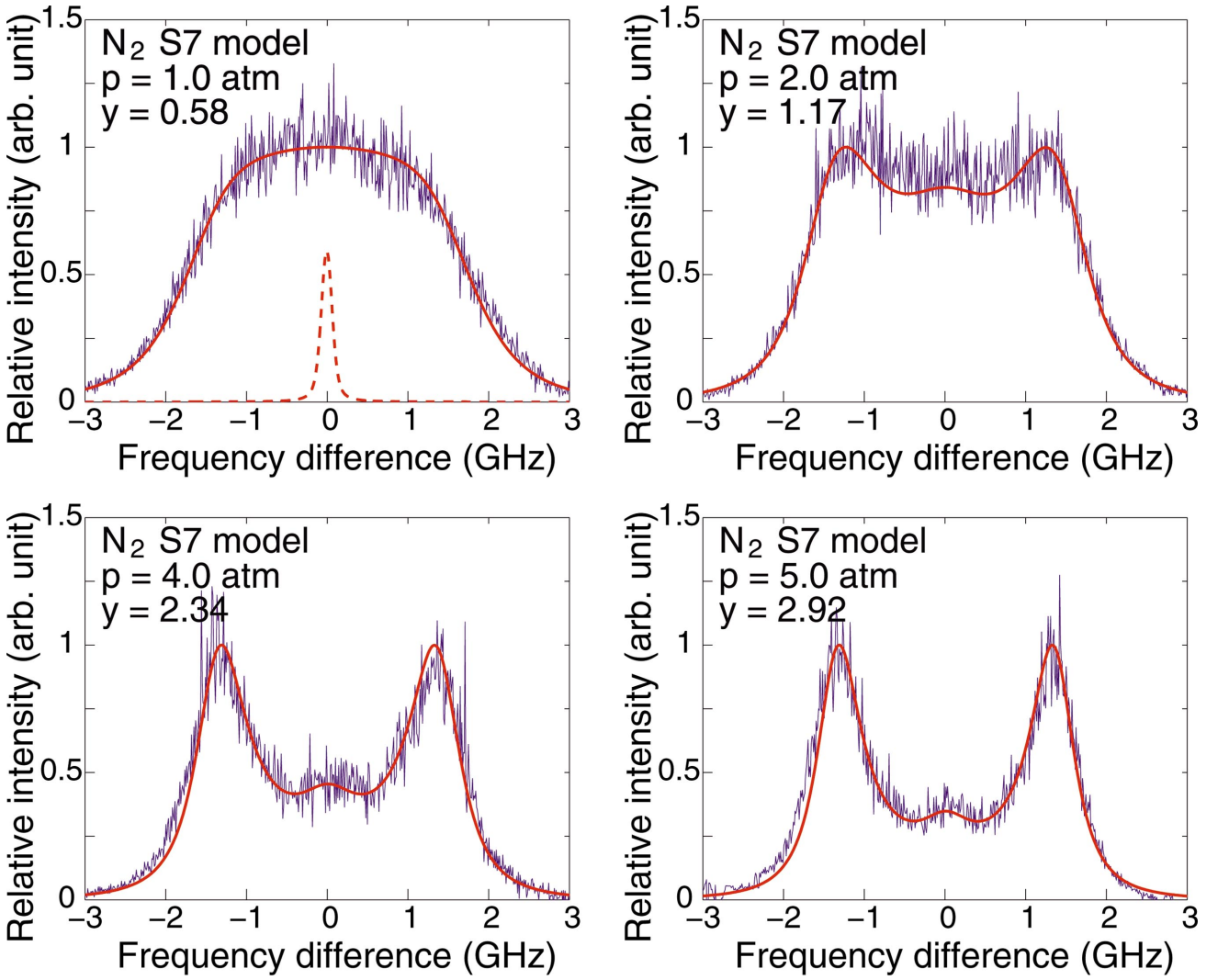

FIG. 4. (Color) Coherent Rayleigh-Brillouin scattering in nitrogen. A comparison between the seven moment molecular gas model with the experimental data. The blue curves are the experimental data, the red curves are the convolution of the instrument function (shown by the dashed red curve in the 1 atm panel) and the theoretical line shape.

In Fig. 5, experimental data in oxygen are compared with the model results. $\eta_b/\eta=1.0$ is used to calculate the model curve. The value found in [39,40] is $\eta_b/\eta=0.4$. The model curve calculated with this value does not match the experimental data. In Fig. 6, the model line shapes with different η_b are compared for oxygen at $y=2.18$. We see that the model is reasonably sensitive to the bulk viscosity. This opens the possibility to measure bulk viscosity using the coherent Rayleigh-Brillouin scattering.

In Fig. 7, the experimental data in carbon dioxide are compared with the seven moment molecular model. The comparison is not satisfactory. For the 1 atm data, the model gives a higher Rayleigh peak. The most serious problem is that at larger y parameters, the $p=3.0$ atm and $p=4.0$ atm panels, the model failed to predict the correct position of the Brillouin peaks. The peak separation of the experimental data at $p=4.0$ atm corresponds to a speed of sound at 283.0 m/s. Available CO_2 data at 4 and 5 atm give a value of the speed of sound as 280.0 ± 5.8 m/s. This value is larger than the values (~259 m/s at 273 K) listed in reference books [35]. The model gives a speed of ~305 m/s, which is significantly larger than the experimental data. Here, a simple fitting by varying the bulk viscosity is insufficient. For a bulk viscosity η_b that is $\sim10^3$ times larger than the shear viscosity η, the position of the Brillouin peak calculated by the model is no longer sensitive to the internal specific heat c_{int}. If one wants to match the Brillouin peaks' separation by using a small $\eta_b/\eta\sim1$, the calculated relative intensity of the Brillouin peaks to the Rayleigh peak is much smaller than the corresponding experimental data.

The mismatch between the model and the experiment in CO_2 indicates that the model needs further development. In CO_2, the vibrational modes come into play. In light diatomic molecules, the vibrational quantum is much higher than room temperature; for example, it is about 3000 K in N_2. The vibrational quantum of polyatomic molecules such as CO_2 is closer to the room temperature (~960 K in CO_2) [37]. It would be of interest to obtain the CRBS data in a wide temperature range in various gases. The data would be useful in the studies of kinetic theory.

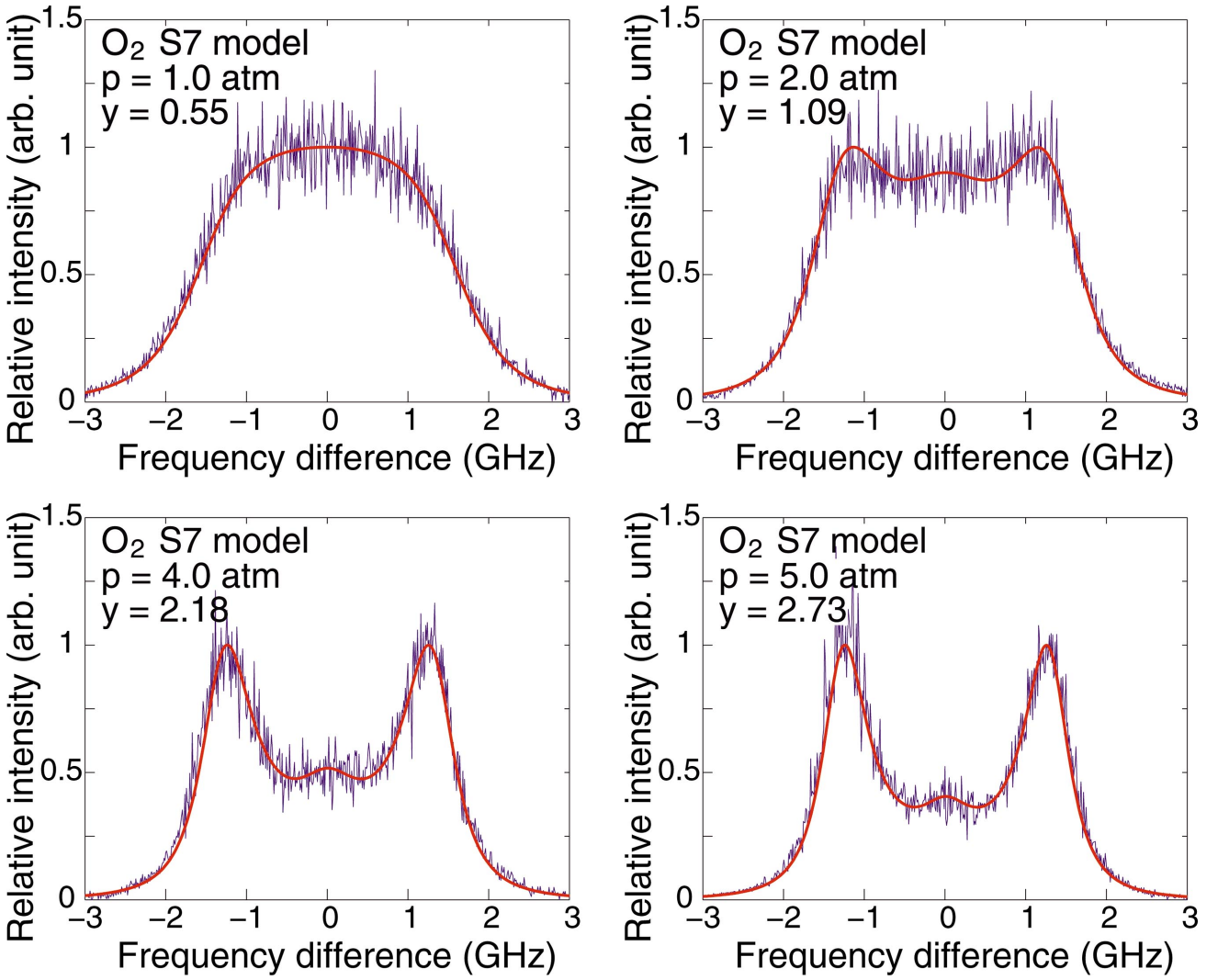

FIG. 5. (Color) Coherent Rayleigh-Brillouin scattering in oxygen. A comparison between the seven moment molecular gas model with the experimental data. The blue curves are the experimental data, the red curves are the convolution of the instrument function and the theoretical line shape. A bulk viscosity $\eta_b = 1.0\,\eta$ is used to calculate the theoretical line shape.

V. MODEL COMPARISON

The molecular CRBS *s*7 and *s*6 models we developed in Sec. IV are also applicable to atomic gases. We suppress the internal modes by setting $\eta_b = 0$ and $c_{\text{int}} = 0$. In the calculation, we actually set $\eta_b = 10^{-3} \times \eta$ and $c_{\text{int}} = 10^{-3}$ to avoid numerical singularity.

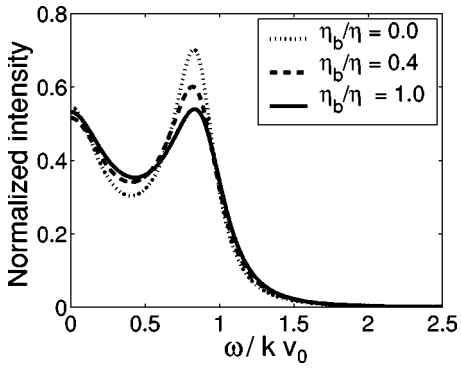

FIG. 6. Coherent Rayleigh-Brillouin scattering line shape in oxygen with different bulk viscosity at $y = 2.18$.

We previously presented an atomic model [9] that matches well with the CRBS data of atomic gases. We now compare the molecular *s*7 model with this atomic model. The two models have different definitions of the y parameter. The way to compare is to use the same optical configuration data and the same gas pressure. For example, with our experimental setup, at $p = 1$ atm, the atomic model y parameter is $y_{\text{mono}} = 0.47$ and the molecular model y parameter is $y = 0.55$. The atomic model requires shear viscosity for the calculation, and the molecular s7 model needs both shear viscosity and thermal conductivity.

Figure 8 shows the comparison using argon shear viscosity and heat conductivity. Four pairs of curves were compared, corresponding to $p = 0$, 1, 3, and 5 atm. For $p = 0$ atm, the two models yield identical results. This is in accordance with our expectation, since, in the collisionless limit, the collision terms do not play a role. For the higher pressure cases,

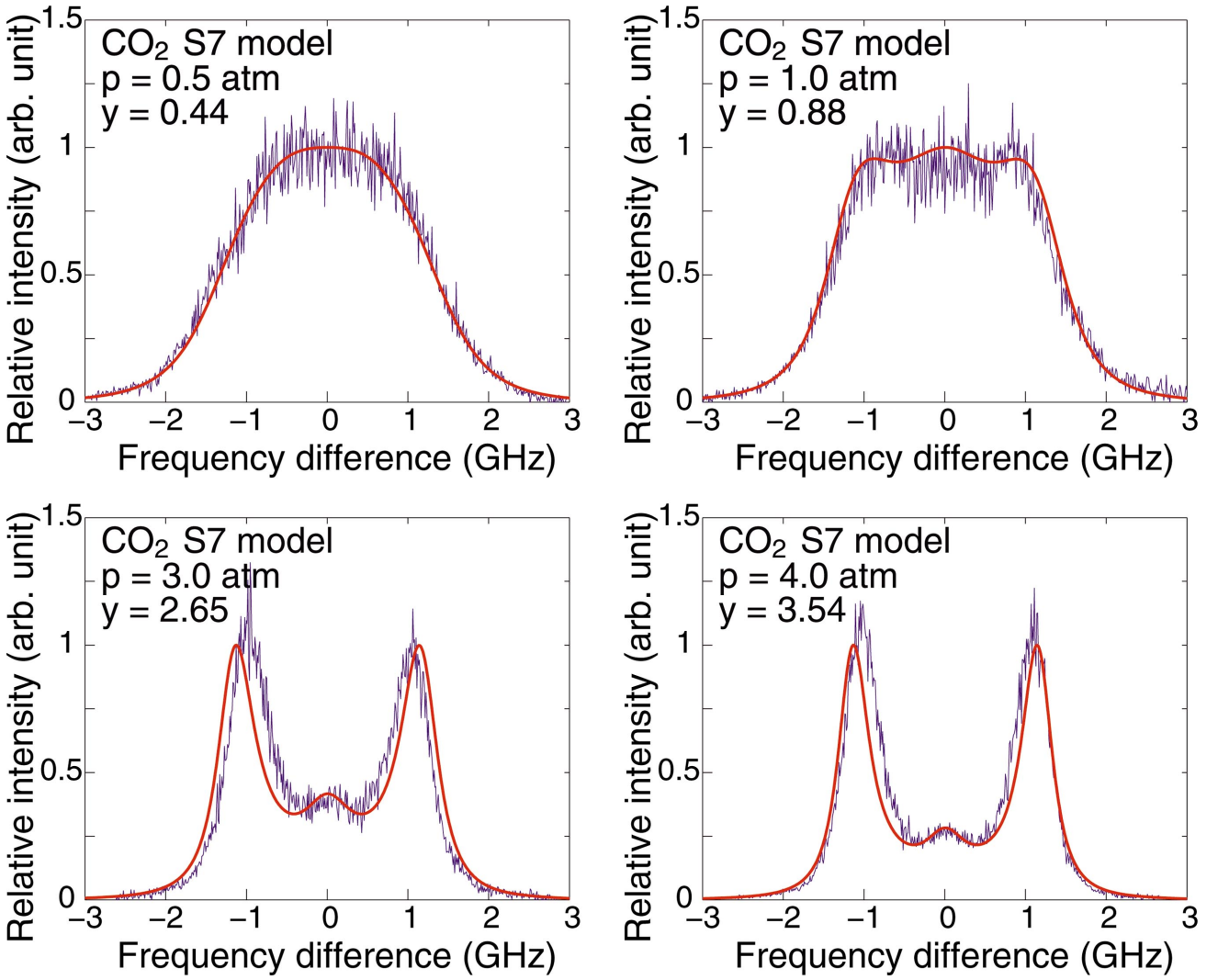

FIG. 7. (Color) Coherent Rayleigh-Brillouin scattering in carbon dioxide. A comparison between the seven moment molecular gas model with the experimental data. The blue curves are the experimental data, the red curves are the convolution of the instrument function and theoretical line shape.

the molecular *s*7 model predicts stronger Brillouin doublets than the atomic model. We have observed in [9] that the atomic model overestimates the Brillouin peaks, therefore, the molecular *s*7 model performance has not surpassed the atomic model for atomic gases.

It is a good place to revisit our y parameter given in [9], we now denote y_{mono} for clarity. Our choice of the y_{mono} parameter does not follow a Chapman-Enskog analysis, which is the basis for most other authors. We followed a more empirical approach by identifying the collision frequency in the BGK model literally and connecting it to the shear viscosity. Such a y_{mono} parameter definition was justified by favorable agreement between the experimental and theoretical line shapes. The match between the *s*7 model and the atomic gas model over a wide kinetic range further supports this choice of y_{mono}.

Next, we compare the *s*7 and *s*6 models. In a subsequent paper, Tenti *et al.* [13] modified their model for the spontaneous Rayleigh-Brillouin scattering. They concluded that the six moment model fits the experimental data better than the seven moment model. Specifically, for $y \sim 1$, their seven moment model shows a weaker Rayleigh peak than the six moment model, with the latter matching better with the observed line shape in HD [13]. Since we have used the same collision terms, it is necessary for us to check the relative performance of the *s*6 and *s*7 models.

In our derivation, the difference between the spontaneous and coherent scattering lies only in the B vector of Eq. (43). For spontaneous scattering, the right-hand side of the matrix equation is given by Eq. (45). In addition, the power spectrum is no longer given by Eq. (5). Instead, it is proportional to the real part of the spontaneous density perturbation $\nu_{spt}(k,\omega)$:

$$\ell_{spt}(k,\omega) \propto \mathrm{Re}[\nu_{spt}(k,\omega)]. \tag{53}$$

The reason for the difference is that, in spontaneous scattering, we solve an initial value problem and a Laplace transform is applied over time; while in coherent scattering, we

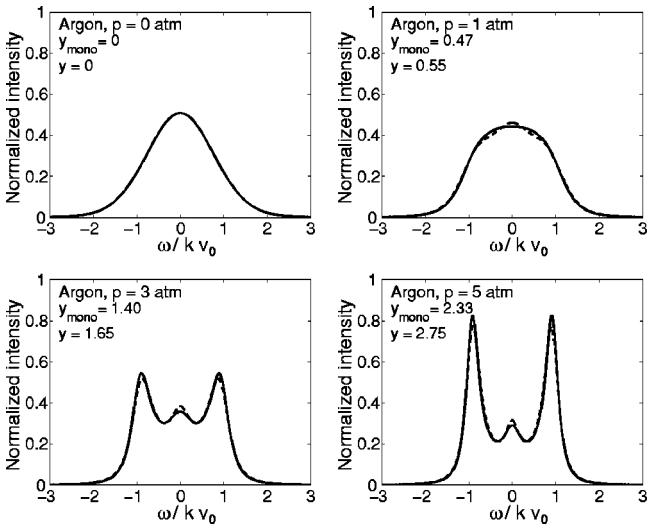

FIG. 8. A comparison between the molecular *s*7 model (solid curve) and the atomic model (dashed curve) for the coherent Rayleigh-Brillouin scattering line shape in N_2. The area under each curve is normalized to 1. The curves are plotted using argon shear viscosity and thermal conductivity at 292 K.

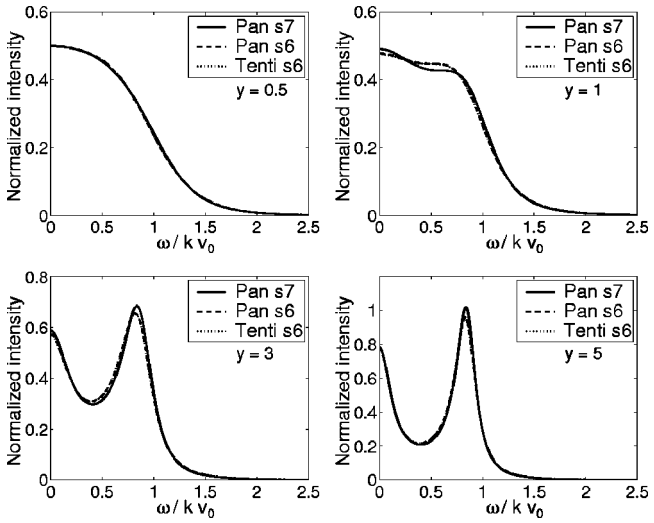

FIG. 9. A comparison of spontaneous Rayleigh-Brillouin scattering line shape by three model programs in N_2. The solid curve is by the seven moment model (Pan *s*7) program, the dashed curve by the six moment model (Pan *s*6) program, and the dotted line by Tenti six moment model (Tenti *s*6) program. The curves by the two six moment model programs completely overlap. The area under each curve is normalized to 1/2.

solve for a steady state solution and a Fourier transform is applied over time.

We first check the difference of *s*6 and *s*7 models for the spontaneous scattering. This way, we can compare our results with that of Tenti *et al.* [13]. Tenti's FORTRAN program of his six moment model is widely circulated. We obtained a copy from Forkey [38]. The program has been slightly modified to adapt to more recent computer operating systems, but the core algorithm remains original. We have used nitrogen dynamics parameters to calculate the curves in this figure. We also compared the model programs using parameters of O_2 and CO_2. A similar difference as shown in Fig. 9 was observed. In general, for spontaneous Rayleigh-Brillouin scattering, the *s*6 and *s*7 models yield identical line shape for $y \lesssim 0.5$. In the range of $0.5 \lesssim y \lesssim 5$, the *s*7 model predicts slightly narrower and higher peaks for both the Rayleigh and Brillouin peaks, representing a less damped perturbation. Our observation of the two model's differences is the opposite of Tenti [13]. They found a sharper Rayleigh peak for HD at $y \sim 1$. The reason for the opposite observation remains unsolved. A possible contradiction, which requires special care, is the calculation of $I_{rl}^{r'l'}$'s. In *s*6 model, they are $I_{rl}^{r'l'}(\xi,y)$, while in the *s*7 model, they are $I_{rl}^{r'l'}(\xi,y_7)$, with $y_7=(3/2)y$.

We now compare the coherent Rayleigh-Brillouin line shapes calculated by the *s*7 and the *s*6 model. We would like to see which model matches the experimental data better. In Fig. 10, we plot the line shape calculate by the seven moment and six moment models. Nitrogen gasdynamics parameters were used in the calculation.

For $y \lesssim 0.2$, the results are indistinguishable. Obvious difference can be seen for $y \sim 1$. For larger y parameters, the seven moment model in general predicts slightly sharper Brillouin peaks, indicating slower dissipation processes. With the uncertainty in bulk viscosities, the data do not show a definitive preference. We feel that more experimental observation is necessary to judge which model is better.

VI. DISCUSSIONS

The experimental configuration of coherent Rayleigh–Brillouin scattering follows a generic four wave mixing experiment. The phase matching scheme can be quite flexible. The data in this paper were collected using a coplanar backward scattering phase matching configuration, illustrated in

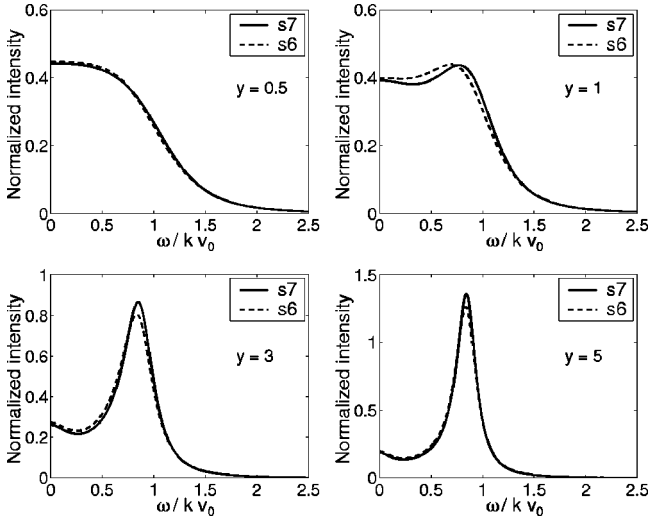

FIG. 10. A comparison of the coherent Rayleigh-Brillouin scattering line shape calculated by the seven moment (*s*7) and the six moment (*s*6) models. The solid curves are calculated by the *s*7 model, the dashed curves by the *s*6 model. The area under each curve is normalized to 1/2.

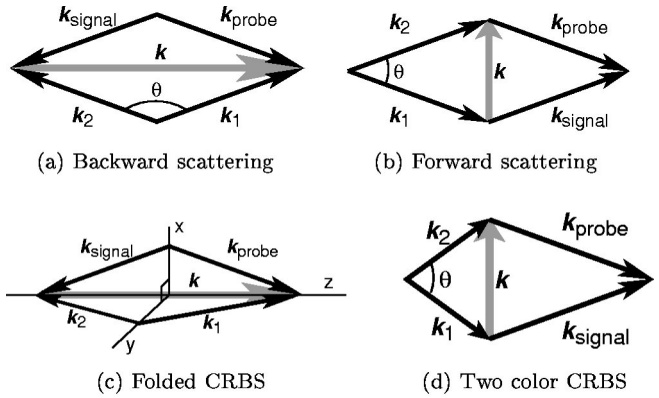

FIG. 11. Phase matching schemes for coherent Rayleigh-Brillouin scattering. $\boldsymbol{k}_1$ and $\boldsymbol{k}_2$ are the pump beams' wave vectors. $\boldsymbol{k}$ is the wave vector of the density perturbation.

Fig. 11(a). With a crossing angle θ near 180°, the fringe pattern has a large wave number k, i.e., a short spatial period. Such a configuration has a strong optical dipole force and a small y parameter.

In Fig. 11(b), we also illustrate a backward scattering, three dimensional, and two-color phase matching scheme. By varying the crossing angle θ, one can access different y parameter for a given gas pressure. The backward scattering configuration is useful when the speed of sound in the gas is of interest.

In the three-dimensional backward scattering scheme shown in Fig. 11(c), the two pump beams ($\boldsymbol{k}_1$ and $\boldsymbol{k}_2$) define a plane. The phonon wave vector lies in this plane and is perpendicular to the equipartition line of the pump beams' crossing angle θ. The probe beam and the signal beam forms a plane that intersects the pump beams' plane along the phonon wave vector. This phase matching scheme is similar to that of a folded BOXCARS [42]. In a 3D phase matching scheme, the signal beam no longer follows one of the pump beams. The perpendicular polarization of the pump beams and the probe beam is no longer necessary. The scheme improves the signal-to-noise ratio since the signal beam is separated in space, however, the alignment of the beams is a little more challenging than in a coplanar scheme. Several scans in room air were performed with this 3D phase matching scheme. The two color configuration shown in Fig. 11(d) is widely used in LITA and LIEG, usually with a cw probe laser. Many experimental issues have been discussed in the literature.

CRBS can be used as a laser diagnostic technique. Together with laser induced thermal acoustics and laser induced electrostrictive gratings, they provide technique capable of making localized and high signal-to-noise ratio measurements of gases from the collisionless limit to the hydrodynamic regime. Further development of CRBS is desirable. In our demonstrative experiments, it takes hundreds of laser shots to scan a high resolution line shape. This limits the use of CRBS in diagnostics where physical processes change quickly. We note that the CRBS signal is sufficiently strong, and a single shot scheme is possible. The challenge would be to resolve the narrow (~6 GHz) line width for the shot. Overall, we expect wide application of CRBS in gas diagnostics.

The CRBS line shape is a result of the balance between laser excitation and collisional relaxation of the gas density perturbation. CRBS data can be a valuable source for the study of kinetic theories. We propose to measure bulk viscosity using coherent Rayleigh-Brillouin scattering in various gases in a wide temperature and pressure range. The unsatisfactory comparison between the theory and the CO_2 data indicate that the theory needs refinement.

In CRBS, the electromagnetic energy of the pump beams is coupled with the kinetic and internal energies of the gas particles at a nonresonant frequency. In this paper, we only considered a small optical dipole force. The potential well produced by the crossing pump beams is much less than the average thermal energy of the gas particles. The perturbation to the gas particles' energy distribution function is small so that the kinetic equation can be linearized. With more intensive pump laser beams, a significant amount of neutral particles may be trapped in the optical lattice, as suggested in [43,44]. A strong optical dipole force field may be used to perturb or transport an ensemble of gas particles at room temperature. When an ensemble of particles is considered, the balanced effects of the optical perturbation and the collisional relaxation may be of interest in recent efforts of optically manipulating nanoscopic particles [45,46].

ACKNOWLEDGMENTS

The author would like to thank Professor G. Tenti of the University of Waterloo and Professor S. H. Lam of Princeton University for useful discussions. This work was supported by the U.S. Air Force Office of Scientific Research under the Air Plasma Rampart Program.

[1] W. A. Schroeder, M. J. Damzen, and M. H. R. Hutchinson, IEEE J. Quantum Electron. **25**, 460 (1989).
[2] H. Tanaka, T. Sonehara, and S. Takagi, Phys. Rev. Lett. **79**, 881 (1997).
[3] C. Y. She, G. C. Herring, H. Moosmuller, and S. A. Lee, Phys. Rev. Lett. **51**, 1648 (1983).
[4] C. Y. She, G. C. Herring, H. Moosmuller, and S. A. Lee, Phys. Rev. A **31**, 3733 (1985).
[5] E. B. Cummings, Opt. Lett. **19**, 1361 (1994).
[6] W. Hubschmid, B. Hemmerling, and A. Stampanoni-Panariello, J. Opt. Soc. Am. B **12**, 1850 (1995).
[7] A. Stampanoni-Panariello, B. Hemmerling, and W. Hubschmid, Phys. Rev. A **51**, 655 (1995).
[8] J. H. Grinstead and P. F. Barker, Phys. Rev. Lett. **85**, 1222 (2000).
[9] X. Pan, M. N. Shneider, and R. B. Miles, Phys. Rev. Lett. **89**, 183001 (2002).
[10] S. Yip and M. Nelkin, Phys. Rev. **135**, 1241 (1964).

[11] P. L. Bhatnagar, E. P. Gross, and M. Krook, Phys. Rev. **94**, 511 (1954).
[12] C. D. Boley, R. C. Desai, and G. Tenti, Can. J. Phys. **50**, 2158 (1972).
[13] G. Tenti, C. D. Boley, and R. C. Desai, Can. J. Phys. **52**, 285 (1974).
[14] C. S. Wang-Chang, G. E. Uhlenbeck, and J. de Boer, in *Studies in Statistical Mechanics*, edited by J. de Boer and G. E. Uhlenbeck (North-Holland, Amsterdam, 1964), Vol. II, Pt. C. The heat conductivity and viscosity of polyatomic gases.
[15] V. Ghaem-Maghami and A. D. May, Phys. Rev. A **22**, 692 (1980).
[16] A. T. Young and G. W. Kattawar, Appl. Opt. **22**, 3668 (1983).
[17] R. B. Miles, W. N. Lempert, and J. Forkey, Meas. Sci. Technol. **12**, R33 (2001).
[18] W. Marques, Jr. and G. M. Kremer, Continuum Mech. Thermodyn. **10**, 319 (1998).
[19] W. Marques, Jr., Physica A **264**, 40 (1999).
[20] A. Rangel-Huerta and R. M. Velasco, Physica A **264**, 52 (1998).
[21] R. W. Boyd, *Nonlinear Optics* (Academic, Boston, 1992).
[22] J. D. Jackson, *Classical Electrodynamics*, 3rd ed. (Wiley, New York, 2000).
[23] B. J. Berne and R. Pecora, *Dynamic Light Scattering* (Wiley, New York, (1976).
[24] X. Pan, P. F. Barker, A. Meschanov, J. H. Grinstead, M. N. Shneider, and R. B. Miles, Opt. Lett. **27**, 161 (2002).
[25] L. D. Landau and E. M. Lifshitz, *Electrodynamics of Continuous Media* (Addison-Wesley, Reading, MA, 1966).
[26] X. Pan, Ph.D. thesis, Princeton University, 2003.
[27] E. A. Mason and L. Monchick, J. Chem. Phys. **36**, 1622 (1962).
[28] L. Monchick, E. A. Mason, and K. Yun, J. Chem. Phys. **39**, 654 (1963).
[29] F. B. Hanson, T. F. Morse, and L. Sirovich, Phys. Fluids **12**, 84 (1969).
[30] T. F. Morse, Phys. Fluids **7**, 159 (1964).
[31] G. Arfken, *Mathematical Methods for Physicists*, 3rd ed. (Academic, New York, 1985).
[32] F. B. Hanson and T. F. Morse, Phys. Fluids **10**, 345 (1967).
[33] E. P. Gross and E. A. Jackson, Phys. Fluids **2**, 432 (1959).
[34] B. D. Fried and S. D. Conte, *The Plasma Dispersion Function* (Academic, New York, 1961).
[35] *CRC Handbook of Chemistry and Physics*, 3rd ed. (Knovel, Norwich, NY, 2000), electronic version.
[36] G. J. Prangsma, A. H. Alberga, and J. J. M. Beenakker, Physica (Amsterdam) **64**, 278 (1973).
[37] G. Emanuel, Phys. Fluids A **2**, 2252 (1990).
[38] J. N. Forkey, Ph.D. thesis, Princeton University, 1996.
[39] C. Truesdell, J. Rat. Mech. Anal. **2**, 643 (1953).
[40] P. A. Thompson, *Compressible-Fluid Dynamics* (McGraw-Hill, New York, 1972).
[41] W. E. Meador, G. A. Miner, and L. W. Townsend, Phys. Fluids **8**, 258 (1996).
[42] A. C. Eckbreth, *Laser Diagnostics for Combustion Temperature and Species*, 2nd ed. (Gordon and Breach, Amsterdam, 1996).
[43] P. F. Barker and M. N. Shneider, Phys. Rev. A **64**, 033408 (2001).
[44] P. F. Barker and M. N. Shneider, Phys. Rev. A **66**, 065402 (2002).
[45] T. Iida and H. Ishihara, Phys. Rev. Lett. **90**, 057403 (2003).
[46] R. R. Agayan, F. Gittes, R. Kopelman, and C. F. Schmidt, Appl. Opt. **41**, 2318 (2002).